Network strain filter: A new tool for monitoring and detecting transient deformation signals in GPS arrays

Ryu Ohtani,[1] Jeffrey J. McGuire,[2] and Paul Segall[3]

Received 4 February 2010; revised 25 June 2010; accepted 2 September 2010; published 22 December 2010.

[1] We have developed a tool to detect transient deformation signals from large-scale (principally GPS) geodetic arrays, referred to as a Network Strain Filter (NSF). The strategy is to extract spatially and temporally coherent signals by analyzing data from entire geodetic networks simultaneously. The NSF models GPS displacement time series as a sum of contributions from secular motion, transient displacements, site-specific local benchmark motion, reference frame errors, and white noise. Transient displacements are represented by a spatial wavelet basis with temporally varying coefficients that are estimated with a Kalman filter. A temporal smoothing parameter is also estimated online by the filter. The problem is regularized in the spatial domain by minimizing a smoothing (Laplacian) norm of the transient strain rate field. To test the performance of the NSF, we carried out numerical tests using the Southern California Integrated GPS Network station distribution and a 3 year long synthetic transient in a 6 year time series. We demonstrate that the NSF can identify the transient signal, even when the colored noise amplitude is comparable to that of transient signal. Application of the method to actual GPS data from the Japanese GPS network (GEONET) on the Boso Peninsula also shows that the NSF can detect transient motions resulting from aseismic fault slip.

Citation: Ohtani, R., J. J. McGuire, and P. Segall (2010), Network strain filter: A new tool for monitoring and detecting transient deformation signals in GPS arrays, *J. Geophys. Res.*, *115*, B12418, doi:10.1029/2010JB007442.

1. Introduction

[2] In the past decade, there has been a tremendous increase in the number and density of geodetic networks for the study of crustal deformation. Large-scale permanent GPS arrays have been developed in Japan (GEONET) [*Hatanaka et al.*, 2003], southern California [*Hudnut et al.*, 2002], the Basin and Range (BARGEN) [*Niemi et al.*, 2004], the Pacific Northwest (PANGA) [*Miller et al.*, 2002], the San Francisco Bay region (BARD) (see, for example, http://gcmd.nasa.gov/records/GCMD_BARD-GPS.html), and elsewhere. In the western United States, 875 continuous GPS receivers are operated by the Plate Boundary Observatory (PBO) as part of the National Science Foundation Earthscope Initiative (for details, see http://pboweb.unavco.org/). These GPS networks yield daily estimates of site positions with a precision of 1–2 mm in the horizontal and 3–4 mm in the vertical over regional distances [e.g., *Zhang et al.*, 1997] and are for the first time providing deformation measurements dense in both space and time. Networks of borehole tilt meters [*Hirose and Obara*, 2005] and strain meters [*Wang et al.*, 2008] provide greater sensitivity at periods shorter than a few weeks and have yielded significant insights into transient processes [e.g., *Hirose and Obara*, 2005, 2006].

[3] For some time, much of the geophysical GPS community's research effort has focused on obtaining accurate interseismic velocities and coseismic displacements (which are reviewed in, for example, *Segall and Davis* [1997] and *Sagiya* [2004a, 2004b]). More recently, transient deformation events have received a great deal of attention. These observations can be modeled as resulting from slip on faults with a rupture velocity much less than the shear wave velocity. Because these so-called slow slip events are nominally invisible to seismic instrumentation yet may release significant elastic strain, they have become the subject of great scientific interest. Slow slip events have now been discovered in Japan [*Hirose et al.*, 1999; *Ozawa et al.*, 2001; *Miyazaki et al.*, 2003; *Ozawa et al.*, 2002; *Miyazaki et al.*, 2006], the Cascadia subduction zone [*Dragert et al.*, 2001; *Miller et al.*, 2002; *Szeliga et al.*, 2008], Mexico [*Lowry et al.*, 2001; *Kostoglodov et al.*, 2003; *Larson et al.*, 2007], Central America [*Norabuena et al.*, 2004], New Zealand [*Douglas et al.*, 2005; *McCaffrey et al.*, 2008; *Delahaye et al.*, 2009], and beneath Kilauea volcano in Hawaii [*Cervelli et al.*, 2002; *Segall et al.*, 2006; *Brooks et al.*, 2006]. It is now recognized that slow slip events in Cascadia and Japan are accompanied by 1–5 Hz seismic signals referred to as "nonvolcanic tremor" [*Rogers and Dragert*, 2003; *Obara*, 2002; *Shelly et al.*, 2007]. The moment magnitudes of these events range from Mw 5.7 beneath Kilauea to greater than Mw 7 in some

[1]Geological Survey of Japan, National Institute of Advanced Industrial Science and Technology, Tsukuba, Japan.
[2]Woods Hole Oceanographic Institution, Woods Hole, Massachusetts, USA.
[3]Department of Geophysics, Stanford University, Stanford, California, USA.

0148-0227/10/2010JB007442

of the subduction zone events [*Kostoglodov et al.*, 2003]. The durations of these events also vary considerably; the Bungo Channel event in southwest Japan lasted roughly 1 year, the Cascadia slow slip event several weeks, the Kilauea silent slip event only 1–2 days, while the Tokai gap, Japan slow slip event lasted roughly 6 years [*Miyazaki et al.*, 2006]. The Cascadia events are known to be episodic, with repeat times of 11–18 months [*Brudzinski and Allen*, 2007; *Schwartz and Rokosky*, 2007]. Previously, slow earthquakes have been identified on the San Andreas Fault from strain and creep meter recordings [*Linde et al.*, 1996].

[4] Transient postseismic deformation is also well established [e.g., *Heki et al.*, 1997; *Hsu et al.*, 2007; *Pritchard and Simons*, 2006]. Deformation in volcanic regions is well known to be episodic, with transient strains preceding some volcanic eruptions. The time scales of preeruptive deformation, however, can be quite variable. For example, permanent GPS stations on Kilauea volcano recorded 8 h of extension prior to a rift eruption in 1997 [*Owen et al.*, 2000]. On the other hand, a network of borehole strain meters showed transient motion only 30 min prior to a basaltic eruption of Hekla in Iceland [*Linde et al.*, 1993].

[5] The large volumes of data provided by modern continuous geodetic networks present both opportunities and challenges. With the order of 10^3 stations, each providing three component positions daily, it is difficult to search for spatially coherent deformation by visual inspection of individual time series. The problem is complicated by the presence of time-dependent noise, due to local benchmark motion and unmodeled atmospheric and other effects. Because of this, it is almost certain that more subtle signals, due to smaller magnitude events, exist in data already collected but have gone undetected. Given the size of the data sets involved and the subtle nature of small transients, it is clear that automated detection algorithms would be very desirable.

[6] In this paper, we present a new method for detecting spatially and temporally coherent signals in data from large GPS arrays, which is referred to as a Network Strain Filter (NSF). The method builds on previous efforts to develop time-dependent methods for inverting geodetic data for slip on faults and dilation of magma bodies, collectively referred to as the Network Inversion Filter (NIF) [*Segall and Matthews*, 1997; *McGuire and Segall*, 2003; *Fukuda et al.*, 2004; 2008]. The NIF is a time domain (Kalman) filter that analyzes all data from a network simultaneously, rather than processing individual time series station by station. This allows the NIF to detect spatially coherent transients from the steady state background strain field. This method has been applied to geodetic data from California [*Segall et al.*, 2000; *Murray and Segall*, 2005], Taiwan [*Hsu et al.*, 2006], Turkey [*Bürgmann et al.*, 2002], Cascadia [*McGuire and Segall*, 2003], Sumatra [*Hsu et al.*, 2006], and Japan [*Aoki et al.*, 1999; *Miyazaki et al.*, 2003; 2006; *Ozawa et al.*, 2001, 2002, 2003, 2005; *Miyazaki and Larson*, 2008], and successfully imaged aseismic fault slip and magma intrusion.

[7] A potential disadvantage of the NIF for detecting strain transients is that it requires one to specify potential sources of deformation, such as faults or magma chambers prior to analysis. While it is possible to develop such models for small areas, doing so for all of Japan or all of western North America is a daunting proposition. Furthermore, if either the model fault geometry or the Green's functions used to relate fault slip to displacement are not fully accurate, the estimate will be biased, and possible transients may be missed. What is needed is a method that identifies spatially coherent transient deformation but does not require source-specific models. This is the intent of the NSF. In the event that an interesting signal is detected, independent data could be sought to confirm the transient, and more detailed modeling, possibly using the NIF, could be undertaken.

[8] In the NSF, GPS time series data are expressed as a sum of steady site velocities, spatially coherent displacements representing transient crustal deformation, spatially uncorrelated benchmark wobble, and reference frame errors. From the displacement time histories, it is possible to derive time-dependent maps of surface displacement, velocity, and strain rate, from which it is possible to detect transient deformation. In our approach, the deformation terms are expanded in a wavelet basis. While other bases could be employed, wavelets are efficient for representing spatially localized processes, and they have proven to be advantageous in estimating deformation fields from GPS data [*Tape et al.*, 2009]. The coefficients of the wavelet basis, along with other time-varying quantities, are estimated by Kalman filtering as in the Network Inversion Filter. The approach outlined here handles data from entire networks simultaneously and thus may be able to detect subtle tectonic signals that are difficult to recognize from individual time series while at the same time requiring no source-specific parameterization.

2. Method

2.1. Formulation

[9] In this section, we present the formulation of NSF for data consisting of time series of station positions from GPS arrays. The extension to time series of EDM or similar differential displacement measurements is obvious. Point strain and tilt data could also be included in a straightforward manner but is not done so here.

[10] The position $\underline{x}$ at time t is expressed as,

$$\underline{x}(t) = \underline{x}(t_0) + \underline{v}\cdot(t-t_0) + \underline{u}(\underline{x},t) + \underline{L}(\underline{x},t-t_0) + \underline{\underline{F}}\,\underline{f}(t) + \underline{\varepsilon}$$
$$\underline{\varepsilon} \sim N\left(0, \sigma^2 \underline{\underline{\Sigma}}_{\mathbf{x}}\right), \tag{1}$$

where $\underline{v}$ represents the secular site velocity, while $\underline{u}(\underline{x},t)$ represents a spatially coherent displacement field. By treating the secular motion at each station independently, we can accurately model arbitrarily short-wavelength variations in this field. An alternative approach is to expand the steady state secular displacements in basis functions as with the transient motions; however, this approach introduces additional parameters and complicates transient detection. The transient displacements $\underline{u}(\underline{x},t)$ include both tectonic and nontectonic (e.g., fluid withdrawal) components. Unlike the NIF, where the source of deformation is explicitly modeled, the NSF does not attempt to distinguish between tectonic and nontectonic transients.

[11] The fourth term in (1), $\underline{L}(\underline{x},t-t_0)$, represents site-specific noise from local benchmark instability, which we model as a Brownian random walk with scale parameter τ (units length time$^{-1/2}$) [*Wyatt*, 1989]. For numerical efficiency, we combine the terms $\underline{x}(t_0)$ and $\underline{L}(\underline{x},t-t_0)$, into a single random walk which initiates at $\underline{x}(t_0)$. The term $\underline{\underline{F}}\,\underline{f}(t)$,

accounts for reference frame errors, where $\underline{\underline{F}}$ is a Helmert transformation and $f(t)$ is a vector of rigid body translations, rotations, and a scale factor [e.g., *Miyazaki et al.*, 2003]. The final term, $\underline{\varepsilon}$, represents observation error, which is assumed to be normally distributed with zero mean and covariance $\sigma^2\underline{\underline{\Sigma}}_x$, where $\underline{\underline{\Sigma}}_x$ is the covariance matrix of the GPS positions provided from GPS analyses and σ^2 is a scale factor to account for unmodeled errors such as those due to multipath or mismodeling of the tropospheric path delays. For numerical efficiency, in the current implementation, τ is assumed to be the same at all GPS stations, although this restriction is easily removed. Many GPS time series record seasonal signals which are believed to result from a combination of soil moisture, hydrologic, and atmospheric loading, and antenna mismodeling. We do not explicitly model seasonal errors in this paper; however, it should not be difficult to incorporate the approach of *Murray and Segall* [2005] in which seasonal terms are modeled with an annual sinusoid with slowly varying amplitude.

[12] The transient tectonic displacements $\underline{u}(\underline{x},t)$ are expanded in spatial basis functions $B(\underline{x})$ with time-varying coefficients $c(t)$,

$$u_i(\underline{x},t) = \sum_m^M B_{im}(\underline{x})\, c_m(t), \tag{2}$$

where the subscript i indexes displacement component and M is the number of basis functions. The coefficients $c(t)$ are modeled as stochastic processes. If the deformation is steady in time, the velocities are constant and $\ddot{c}_m$, $m = 1, \ldots, M$, vanishes (the overdot indicates time derivative). For a nearly steady state process, we model the accelerations by a stochastic process with mean zero and variance α^2. In particular, following *Segall and Matthews* [1997] we assume the transient velocities follow a random walk, which implies

$$\dot{c}(t) = \alpha \int_0^t \mathrm{d}\omega(t'), \tag{3}$$

where $\omega(t)$ is an independent white noise process $\omega \sim N(0, I)$ and the constant of integration is absorbed into the secular site velocities. The coefficients $c(t)$ are thus given by integrating (3),

$$c(t) = \alpha w(t), \tag{4}$$

where $w(t)$ is an integrated random walk [e.g., *Segall and Matthews*, 1997]. The integration constant here is absorbed in the term $\underline{x}(t_0)$. Combining equations (2) and (4), the tectonic displacement term in (1) can thus be written as

$$u_i(\underline{x},t) = \alpha \sum_m^M B_{im}(\underline{x})\, w_m(t). \tag{5}$$

All of the time-varying quantities, including the coefficients $w(t)$, the random walk estimates, and reference frame corrections are estimated using Kalman filtering techniques [e.g., *Brown and Hwang*, 1997], as in the NIF. By choosing a nonparametric representation of the coefficients $w(t)$, we allow the data rather than a priori assumptions determine the time-varying nature of the transient deformation. The hyperparameter α controls the temporal smoothing of the transient displacements and can be estimated in the filter using an extended Kalman filtering algorithm as discussed by *McGuire and Segall* [2003]. In this work we assume that α is constant in space and time. *Fukuda et al.* [2004; 2008] present methods for incorporating time-varying α, which does a better job of capturing abrupt transients. Their methods are computationally intensive and are not implemented here, where our principal goal is to identify subtle rather than abrupt transients; however, future work could incorporate this filtering approach.

2.2. Choice of Wavelet Functions

[13] In this section, we consider the choice of basis functions $B(x)$. Several commonly used functions, such as Fourier series, are not well suited because they have global support (that is, they are nonzero over the entire spatial domain) and thus require many terms to represent localized deformation due, for example, to volcanic inflation, or buried fault slip. We require basis functions that are suitable for expressing localized deformation in a large geodetic array. Specifically, the functions should have nonzero values only over a localized area. Furthermore, the basis should be differentiable, so that the resulting strain distribution is well defined.

[14] While other choices such as splines or empirical orthogonal functions could be considered, in this study we use wavelet functions as a spatial basis to represent transient deformation, $\underline{u}(\underline{x},t)$. Here we briefly overview some basic properties of wavelets, starting with the one-dimensional case. For geophysical examples, see *Addison* [2002], *Kumar and Foufoula-Georgiou* [1994], and *Kumar and Foufoula-Georgiou* [1997].

[15] A wavelet $\psi(x)$ is a wave-like function with unit 2-norm $\int|\psi(x)|^2\,\mathrm{d}x = 1$ [e.g., *Mallet*, 1998]. The Deslauriers-Dubuc wavelet of degree 3 (will be explained below) is shown in Figure 1 as an example of one-dimensional wavelet. A family of wavelet functions $\{\psi_{j,k} \mid j,k \in \boldsymbol{Z}\}$ (where $\boldsymbol{Z}$ is the set of integers) can be formed by dilating (or contracting) and translating a unit wavelet ψ, which is sometimes called an analyzing or mother wavelet. One such realization of a discrete, dyadic wavelet family is

$$\psi_{j,k}(x) = 2^{-\frac{j}{2}}\psi\left(\frac{x - k2^j\Delta x}{2^j}\right) \quad j,k \in \boldsymbol{Z}. \tag{6}$$

The indices j and k refer to different scales and shifts, respectively, and $\Delta x > 0$ is the discretization increment [*Kumar and Foufoula-Georgiou*, 1997].

[16] Orthogonal wavelets, which are orthogonal to all of their translates and dilates [*Mallet*, 1998], have desirable properties. In particular all square integrable functions $g(x)$ can be represented to arbitrary precision by a linear combination of the form,

$$g(x) = \sum_{j=-\infty}^{\infty}\sum_{k=-\infty}^{\infty} \psi_{j,k}(x)\, q_{j,k}, \tag{7}$$

where $q_{j,k}$ are coefficients. Note that as the scale gets larger, that is increasing j, the number of translations and thus the number of coefficients decrease.

[17] Orthogonal wavelets typically lack simple closed form expressions in the spatial domain and are defined only on a

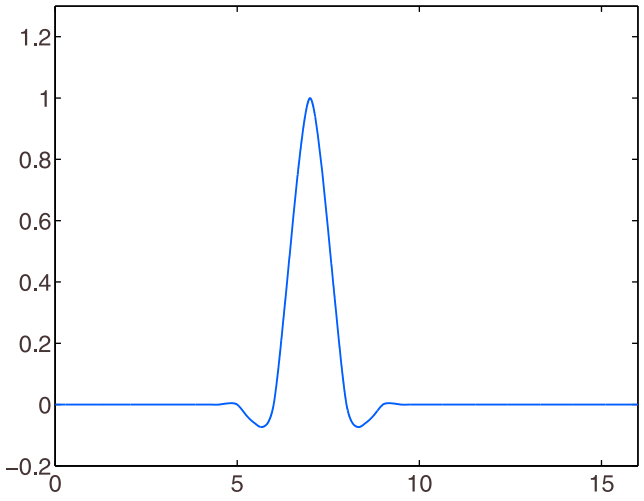

Figure 1. One-dimensional Deslauriers-Dubuc wavelet of degree 3.

regular grid. The distribution of GPS stations in the real world, however, is irregularly spaced. Simply calculating the value of an orthogonal wavelet for irregularly spaced points is not as simple as it is for some nonorthogonal wavelets that have closed form expressions. We proceed as follows; orthogonal wavelets are obtained by solving two-scale difference equations that provide values on a dyadic grid [*Daubechies*, 1992]. By setting the spacing of this dyadic grid to be sufficiently small to allow us to linearly interpolate between the grid points, we are able to calculate values at arbitrary points with reasonable precision.

[18] An advantage of orthogonal wavelets is that it enables the introduction of a scaling function (or "father wavelet") and so-called multiresolution analysis (MRA). When we introduce a scaling function $\phi(x)$, the terms with higher scales ($j \geq j_0$) in the expansion (7) in terms of the analyzing wavelet can be replaced by a single scaling function (at scale j_0). Namely, with no loss of information, (7) can be written as,

$$g(x) = \sum_{k=-\infty}^{\infty} \phi_{j_0,k}(x)\, q^{s}_{j_0,k} + \sum_{j=-\infty}^{j_0} \sum_{k=-\infty}^{\infty} \psi_{j,k}(x)\, q^{a}_{j,k}, \qquad (8)$$

where

$$\phi_{j,k}(x) = 2^{-\frac{j}{2}} \phi\left(\frac{x - k2^j \Delta x}{2^j}\right) \quad j,k \in \boldsymbol{Z}, \qquad (9)$$

and $q^{s}_{j,k}$ and $q^{a}_{j,k}$ represent the coefficients of the scaling function and analyzing functions for the given scale and translation, respectively. It should be noted that dilates and translates of the scaling function $\{\phi_{j,k} \mid j, k \in \boldsymbol{Z}\}$ also form an orthogonal basis. In (8) all of the terms above the scale j_0 are replaced with a single scaling function (see Appendix A). In practice we represent the displacements with finite sums of the form of equation (8). Choosing j_0=0 and a minimum wavelet scale $j_{\min}$, then $j = j_{\min}, \ldots, -2, -1, 0$, and $k = 0, 1, 2, \cdots, 2^{-j_{\min}} - 1$.

[19] We examined several wavelets to use as a basis for this analysis. Among wavelets, wavelets from the Deslauriers-Dubuc interpolating scheme (hereafter referred to as DD wavelet) are advantageous. Though they are not exactly orthogonal, they are suitable for MRA, have compact support, and are smooth [*Sweldens and Schröder*, 1996]. DD wavelets of degree $2p - 1$ are constructed to have compact support over $[-2p+1, 2p-1]$ [see *Mallet*, 1998; *Sweldens and Schröder*, 1996]. For $p = 1$, the wavelet is a piecewise linear function. When $p = 2$, the wavelet is smoother, with a somewhat Gaussian shape. As p gets larger, the support increases. We have found that the DD wavelet with $p = 2$ (degree 3) is a reasonable compromise between the size of the compact support and the computational burden of calculating the wavelet. The one-dimensional DD wavelet is illustrated in Figure 1.

[20] An alternative approach is to use nonorthogonal wavelets, such as the Mexican hat wavelet (second derivative of the Gaussian). The advantage of nonorthogonal wavelets is that they often have explicit analytical forms and are therefore easier to compute. A disadvantage of nonorthogonal wavelets is that they do not have the decomposition (8) and therefore care is needed at the longest spatial scales. While not reported here, we have also conducted numerical experiments with nonorthogonal wavelets that achieve comparable results to those presented here with the DD orthogonal wavelets.

[21] In this work, we analyze only the horizontal displacements, although the method can be simply extended to include the (noisier) vertical component. At present we neglect earth curvature, such that the east and north components of displacement are expressed as functions of Cartesian coordinates, $u_E(x_E,x_N,t)$ and $u_N(x_E,x_N,t)$. An alternative approach would be to use spherical wavelets, as in the work of *Tape et al.* [2009], which are advantageous for networks with a large spatial extent. Spherical wavelets have proven successful in estimating static velocity and strain fields from geodetic data sets [*Tape et al.*, 2009]. Wavelets on a sphere also more naturally represent the data in geodetic coordinates, i.e., east and north components.

[22] We assume a separable isotropic basis, so that two-dimensional wavelets are constructed as tensor products of corresponding one-dimensional wavelets. As explained in Appendix B, the two-dimensional representation includes tensor products of (1) wavelets in the east direction with wavelets in the north direction, (2) wavelets in the east direction with scaling functions in the north direction, (3) wavelets in the north direction with scaling functions in the east direction, and (4) scaling functions in east and north directions. The transient deformation term from equation (5) can thus be expressed as

$$\begin{aligned}\sum_{m}^{M} B_{im}(x_E,x_N)\, w_m(t) = &\sum_{k_1}\sum_{k_2} \Phi^{s}_{j_0,k_1,k_2}(x_E,x_N)\, w^{s}_{j_0,k_1,k_2}(t) \\ &+ \sum_{j=j_{\min}}^{j_0}\sum_{k_1}\sum_{k_2} \Psi^{e}_{j,k_1,k_2}(x_E,x_N)\, w^{e}_{j,k_1,k_2}(t) \\ &+ \sum_{j=j_{\min}}^{j_0}\sum_{k_1}\sum_{k_2} \Psi^{n}_{j,k_1,k_2}(x_E,x_N)\, w^{n}_{j,k_1,k_2}(t) \\ &+ \sum_{j=j_{\min}}^{j_0}\sum_{k_1}\sum_{k_2} \Psi^{d}_{j,k_1,k_2}(x_E,x_N)\, w^{d}_{j,k_1,k_2}(t)\end{aligned} \qquad (10)$$

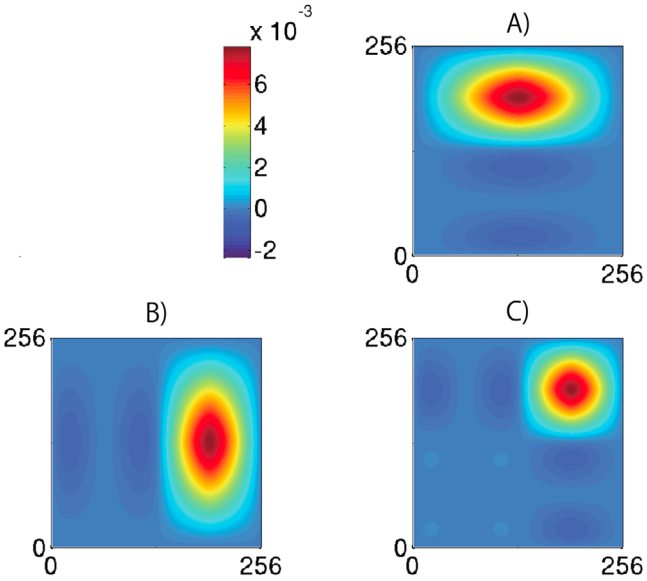

Figure 2. An example of the two-dimensional Deslauriers-Dubuc wavelet of degree 3 with the scale $j = -1$. (a) East-west analyzing wavelet, Ψ^e. (b) North-south analyzing wavelet, Ψ^n. (c) Diagonal analyzing wavelet, Ψ^d.

where $j_{\min}$ and j_0 ($j_{\min} \le j_0$) are the minimum and maximum scales, respectively. $\Phi^s_{j_0,k_1,k_2}$ is the two-dimensional scaling function, and Ψ^e_{j,k_1,k_2}, Ψ^n_{j,k_1,k_2}, and Ψ^d_{j,k_1,k_2} are the three two-dimensional analyzing wavelets (which we refer to as east-west, north-south, and diagonal analyzing wavelets; see Appendix B for details), and w^s_{j0,k_1,k_2}, w^e_{j,k_1,k_2}, w^n_{j,k_1,k_2}, and w^d_{j,k_1,k_2} are coefficients. Owing to the property of the MRA, we can set the maximum scale to an arbitrary integer; thus, we hereafter set the maximum scale j_0 to be zero; all signals at longer spatial wavelengths are included in the scaling function $\Phi^s_{j_0,k_1,k_2}$. Given the periodic (wraparound) condition, where wavelets that spill over at one side of the boundary are wrapped around at the other side, the scaling function, $\Phi^s_{j=0}$ becomes constant [*Addison*, 2002]. The three analyzing wavelets are illustrated in Figure 2 for the DD wavelet at the scale, $j = -1$. Note that the number of translations, k_1 and k_2, are functions of the scale j, as they are in the one-dimensional case.

2.3. Minimum Scale and Regularization

[23] As discussed in section 2.2, the number of translations is limited by the extent of geodetic array. Some consideration, however, is needed to choose the minimum and maximum wavelet scales. The largest scale is set by the extent of the geodetic array in latitude and longitude; the analyzing wavelets are contracted to represent smaller-scale structures. The choice of minimum scale wavelet is determined by the station spacing. Choosing a minimum scale that is too small results in mapping local noise processes into deformation, leading to spurious estimates of transient deformation. At the extreme, there is no point in including wavelets that do not span any geodetic stations. Even excluding this case, there are generally more wavelet coefficients than there are stations: the problem is strictly underdetermined.

[24] To produce a smooth strain field that satisfies the geodetic observations thus requires some weighting of the wavelet coefficients. We regularize the otherwise underdetermined estimation problem by minimizing a spatial norm of the transient strain rate field, $\lambda^2 \, \|\dot{\varepsilon}(x)\|^2_S$, where $\dot{\varepsilon} = \partial \dot{u}/\partial x$ (for the time being we consider one-dimension only; tensor components are discussed below), the subscript S indicates a smoothing norm, and λ^2 is a scalar. We define a second derivative, smoothing (semi-) norm as

$$\| f(x) \|^2_S \equiv \langle f(x), f(x) \rangle = \int_{-\infty}^{\infty} (f''(x))^2 \mathrm{d}x$$

$$\text{where } \langle f(x), g(x) \rangle \equiv \int_{-\infty}^{\infty} f''(x) g''(x) \mathrm{d}x, \tag{11}$$

and prime indicates spatial derivative. Expanding the transient strain rate field in spatial basis as in (2),

$$\dot{\varepsilon}(x,t) = \sum_{m}^{M} B'_m(x) \dot{c}_m(t), \tag{12}$$

the norm of the strain rate field can thus be written as

$$\| \dot{\varepsilon}(x) \|^2_S = \dot{c}^T \Gamma \dot{c}, \tag{13}$$

where the components of the Gram matrix Γ are given by $\Gamma_{ij} = \langle B'_i, B'_j \rangle$. Here $\langle , \rangle$ indicates the inner product associated with the smoothing norm in (11). It should be noted that because the norm in (13) is a derivative norm, the orthogonality of the wavelets does not imply that the Gram matrix is the unit matrix, in fact it is not.

[25] Given a wavelet basis of the form (6), the inner products that yield the components of the Gram matrix are of the form

$$\left\langle \frac{\partial \psi_{j,k}}{\partial x}, \frac{\partial \psi_{m,n}}{\partial x} \right\rangle = \left\langle 2^{-j/2} \frac{\partial}{\partial x} \psi\left(\frac{x}{2^j} - k\Delta x\right), 2^{-m/2} \frac{\partial}{\partial x} \psi\left(\frac{x}{2^m} - n\Delta x\right) \right\rangle$$
$$= 2^{-(j+m)/2} \left\langle \frac{\partial}{\partial x} \psi\left(\frac{x}{2^j} - k\Delta x\right), \frac{\partial}{\partial x} \psi\left(\frac{x}{2^m} - n\Delta x\right) \right\rangle. \tag{14}$$

For general j, m, and k, n, the resultant inner product may have to be integrated numerically. Note however, that because wavelets have compact support, the inner product will vanish for wavelets of the same scale ($j = m$) and offset greater than the wavelet's support.

[26] To the extent possible given the data, a smooth solution maps the signal into the longer wavelength spatial scales. Thus, of particular interest is the contribution to the Gram matrix from wavelets at the same offset but different scales. This determines how the different spatial scales should be weighted in the estimation. For $j = m$, $k = n$, and the second difference seminorm (11), equation (14) becomes

$$\left\langle \frac{\partial \psi_{j,k}}{\partial x}, \frac{\partial \psi_{j,k}}{\partial x} \right\rangle = 2^{-j} \int_{-\infty}^{\infty} \left(\frac{\partial^3}{\partial x^3} \psi\left(\frac{x}{2^j} - k\Delta x\right) \right)^2 \mathrm{d}x. \tag{15}$$

Making the substitution $\xi = 2^{-j}x - k\Delta x$ and applying the chain rule yields

$$<\frac{\partial \psi_{j,k}}{\partial x}, \frac{\partial \psi_{j,k}}{\partial x}>= 2^{-6j} \parallel \psi'(\xi) \parallel_S^2 = 2^{-6j} \int_{-\infty}^{\infty} (\psi'''(\xi))^2 d\xi. \quad (16)$$

As made explicit here, the norm and associated inner product imply spatial differentiation of the wavelets. Equation (16) shows that weighting the different wavelet scales by 2^{-6j} is appropriate given the specified smoothing norm and associated inner product. The integral in (16) represents the squared norm of the gradient of the analyzing wavelet. The Gram matrix also includes terms related to the inner product of wavelets at different scales and offsets. For the current study, we have not computed the full Gram matrix, rather approximating it with a diagonal matrix with entries of the form (16). With this approximation, it is not actually necessary to compute the integral in (16), as this value can be absorbed into the scalar λ^2.

[27] In two dimensions, we employ a Laplacian (semi) norm

$$\parallel f(x,y) \parallel_S^2 = \int_{-\infty}^{\infty} \int_{-\infty}^{\infty} \left(\nabla^2 f(x,y)\right)^2 dx dy. \quad (17)$$

In a two-dimensional case, each component is expanded in four sets of sums, as in equation (10). However, due to the distributive property of the inner product, this simply results in (many) more terms in the computation of each entry in the Gram matrix. Also, as discussed in Appendix B, we form two-dimensional wavelets as tensor products of one-dimensional wavelets. Importantly, the norm of any component of the strain rate or any linear combination of strain rate components such as the areal dilatation rate will involve spatial (partial) derivatives of order three – one from the definition of strain and two from the second derivative smoothing. Thus, the norm of any of the surface strain rate components at the same scale and offset scales with 2^{-6j} as in one dimensional. In contrast, first derivative smoothing of the strain rate field scales with 2^{-4j}. Our numerical tests indicate better results with second derivative smoothing, so that is employed here. With a diagonal approximation of the Gram matrix, the definite integrals of the analyzing wavelets and scaling functions can be absorbed into the smoothing parameter λ^2, as in the one-dimensional case. While one presumably achieves better results by numerically computing the full Gram matrix, we have not attempted to do so.

2.4. Kalman Filtering

[28] The unknowns to be estimated at each observation epoch include the secular velocity at each station, the coefficients representing the transient displacement field, the random walk benchmark components, the reference frame parameters, and the temporal smoothing hyperparameter (α). All of these are incorporated into the state vector $\underline{X}$ that is estimated by the extended Kalman filter (Appendix C). The total number of parameters estimated at each epoch is 4*M (M = number of basis functions, times 2 components of displacement, times 2 coefficients/basis) + 2*N (for the secular velocity of each component) + 2*N (for benchmark wobble at each station) + 2 (reference frame translations in each component) + 1 (the hyper parameter α). The total number of basis functions M is 1 (for the scaling function) + 3*(number of scales; $j_0 - j_{\min} + 1$)*(number of wavelet translations at each scale (for Ψ^e, Ψ^n, and Ψ^d)). However, in practice, we do not include basis functions that are poorly observed by a particular network in the estimation. For the studies shown below, we have only included basis functions which have an amplitude of $\geq 10\%$ of the peak amplitude at ≥ 5 stations. *Tape et al.* [2009] followed a similar selection approach in estimating continuous velocity fields from discrete data using wavelet basis functions.

[29] The state vector at all epochs is estimated through an extended Kalman filter, a recursive least squares estimator. The state at epoch k, given data up to that epoch is written as $\underline{X}_{k|k}$, with covariance matrix $\underline{\underline{C}}_{k|k}$. The state at epoch $k+1$ is predicted based on the stochastic state evolution equations yielding, $\underline{X}_{k+1|k}$. New data at epoch $k+1$ is incorporated in a weighted least square sense, leading to an updated state. This state is conditional on data up to epoch $k+1$, written as $X_{k+1|k+1}$ with covariance $\underline{\underline{C}}_{k+1|k+1}$. These estimates, based on all available data up to the current epoch, are referred to as filtered estimates. The process iterates until the final data epoch; if there are N_e epochs, this yields $\underline{X}_{N_e|N_e}$. Smoothed estimates, conditional on all data, $\underline{X}_{k|N_e}$, are obtained by backward application of the Kalman filter (see Appendix C).

[30] Following *Segall and Matthews* [1997] the regularization is introduced in the Kalman filter through the a priori state $\underline{X}_{1|0}$ and covariance, $\underline{\underline{C}}_{1|0}$, that is, the state prior to the first observations [see *Segall and Matthews*, 1997; equation (50)]. For the transient velocity coefficients, the $\dot{c}$ terms in equation (3), we set the prior state to zero, and the corresponding components of the prior covariance matrix to $\underline{\underline{C}}_{1|0} = \frac{1}{\lambda^2} diag(2^{6j})$, where *diag* indicates a diagonal matrix, and $1/\lambda^2$ weights spatial smoothing relative to fitting the data. That is, all wavelet coefficients are a priori set to zero, but that the confidence in this is least for the longest wavelength spatial scales. Thus, the coefficients only move away from zero if the data demand. The coefficients corresponding to the transient *displacement* on the other hand are set to zero, with very small variance, 1e-8 m^2, because at time $t = 0$, there has been no time for transient displacement to accumulate. The secular site velocities are also initialized at zero, but with very broad prior uncertainty (0.05 m/yr). For the reference frame terms the $\underline{\underline{C}}_{1|0}$ terms are set to 1e-4 m^2, which is sufficient in our experience to absorb frame errors in actual data sets. For the random benchmark motion term, we set $\underline{\underline{C}}_{1|0}$ terms to 1e-4 m^2, which as explained above accounts for uncertainty in the site position at the initial epoch. For the synthetic tests conducted here the random walk error is taken to be 3 mm/$yr^{1/2}$.

[31] The prior estimate and variance of the temporal smoothing parameter α requires some consideration. In our experience a poor choice of α can lead to instability in the extended Kalman filter. Our implementation actually propagates $\log(\alpha)$, which has the benefit of keeping this quantity nonnegative. In the simulations here, we initialize the filter with a small value, e.g., $\log(\alpha)_{1|0}=-9$ with large variance $\mathrm{Var}[\log(\alpha)]_{1|0}=7$. This allows sufficient leeway for the temporal smoothing parameter to adapt to transients. In practice for a given data set, the prior value of α has to be adjusted so that it implies a nearly steady transient field, such

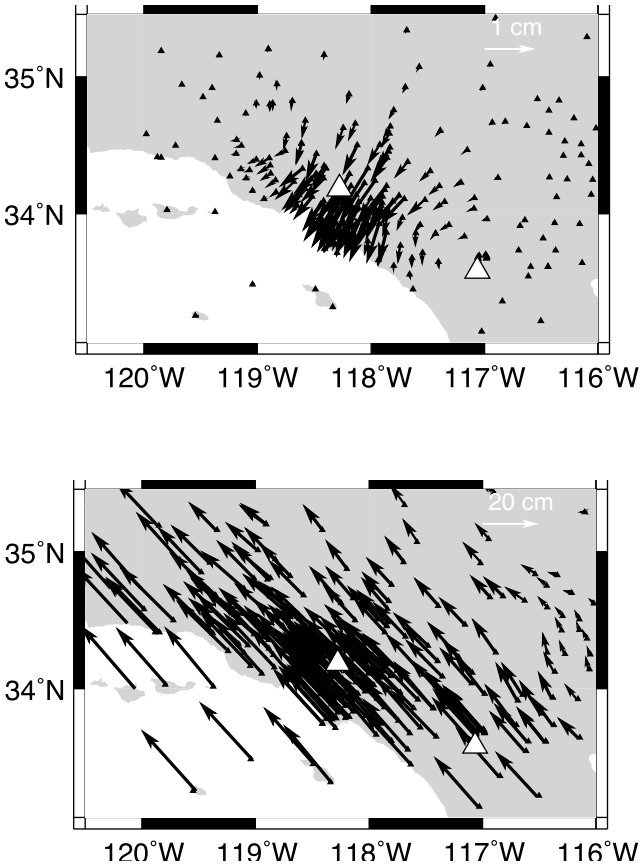

Figure 3. Simulation using the station distribution of the Southern California Integrated GPS Network (SCIGN, black triangles). The black vectors show the distribution of the (top) transient and (botom) secular displacement at the final epoch at all GPS stations. White arrows give the scale in each plot; note that the magnitude of the secular field is significantly larger than that of the transient field. The two white triangles give the locations of stations BILL (southeast triangle) and BRAN (middle triangle).

that any actual transients will force the estimate of α to increase [*McGuire and Segall*, 2003].

[32] As a check on the filtered estimates, the residual variance should be consistent with that expected given the nominal errors in the data. From equation (1) the predicted data is given by

$$\hat{\underline{x}}(t) = \hat{\underline{x}}(t_0) + \hat{v} \cdot (t - t_0) + \hat{\underline{u}}(\underline{x}, t) + \underline{\underline{F}}\,\hat{\underline{f}}(t), \tag{18}$$

where the hat indicates predicted value. Thus, the residual variance in the station positions should be

$$\mathrm{var}(\underline{x}(t) - \hat{\underline{x}}(t)) \sim \mathrm{var}\left\{(\underline{L}(\underline{x}, t) + \underline{\varepsilon})^{apriori}\right\} = \tau^2(t - t_0) + \sigma^2 \underline{\underline{\Sigma}}_x, \tag{19}$$

since the benchmark motions and white noise are assumed uncorrelated. One can check the filter residuals to ensure that this is reasonably well satisfied. It should be noted however that residuals satisfying (19) does not prove that the filter has correctly resolved the signal into its constituent components, transient displacement, random walk, reference frame error, etc. The various components of the state vector must be examined a posteriori to demonstrate consistency with the model assumptions.

3. Synthetic Test

[33] We carried out simulations to test the performance of the filter by analyzing synthetic GPS data. We generated synthetic data for a network with the geometry of the South California Integrated GPS Network (SCIGN) with 219 stations. We set a hypothetical buried fault, 250 km long and 20 km wide, with a dip of 10 degrees running along the strike of the San Andreas Fault. This was not chosen to represent a known structure, but rather to simply generate a coherent transient field. We generated a 6 year long synthetic time series, with a slow slip event starting in year two and lasting for three years that produced a transient displacement field concentrated in the L.A. basin (Figure 3). The signal amplitude was chosen such that the peak amplitude of the transient field is similar to the amplitude of the benchmark wobble, but both are much smaller than the secular field (Figure 3). The time history of slip is imposed such that resultant displacement has a gradual (slow) initialization, followed by rapid growth, and ends gently. The station displacements are computed from the transient slip using Green's functions for homogeneous elastic half-space. Secular motion is added based on actual SCIGN data. Finally, we add local benchmark motion, modeled as a random walk process with a scale parameter of 1.5 mm/yr$^{1/2}$, and measurement errors, assumed to be Gaussian white noise with a scale of 2 mm. Because of the long duration of the event, the contributions from secular motion and benchmark wobble make it difficult to identify the transient signal by eye in individual records.

[34] Figure 4 illustrates the locations and dimensions of the wavelets used to represent the transient deformation field. Note that there are many wavelets at the smallest scale and that the number of small scale wavelets depends on the station density.

[35] The primary decision to be made in analyzing the synthetic data set is the choice of the prior covariance matrix for the state vector. We follow the procedure described in section 2 which is straight-forward for the elements corresponding to the transient displacement, the secular velocity, the benchmark wobble, and the frame translations. For α, we chose a prior ($\log(\alpha)_{110} = -9$; $\mathrm{Var}[\log(\alpha)]_{110}$=7) that corresponds to the a priori assumption that there are no significant transient displacements but allows the freedom for the estimate of α to increase if required by the data. To estimate the smoothing weight λ^2, we ran the filter for a number of values of λ^2 and calculated the model norm of the resulting transient strain field (the two-dimensional extension of equation (13), but with $\boldsymbol{c}$ rather than its time derivative) at the final epoch. The tradeoff between the roughness of the transient field and the magnitude of λ^2 is very strong (Figure 5). This tradeoff arises because small values of λ^2 allow the secular field to be mapped into the transient field. In the limit that λ^2 is extremely small, there is no need for the elements of the state vector corresponding to the secular field, because the entire signal can be mapped into an arbitrarily rough transient field. This can be seen in the temporal evolution of the filtered estimate of α for different values of λ^2 (Figure 6). For small

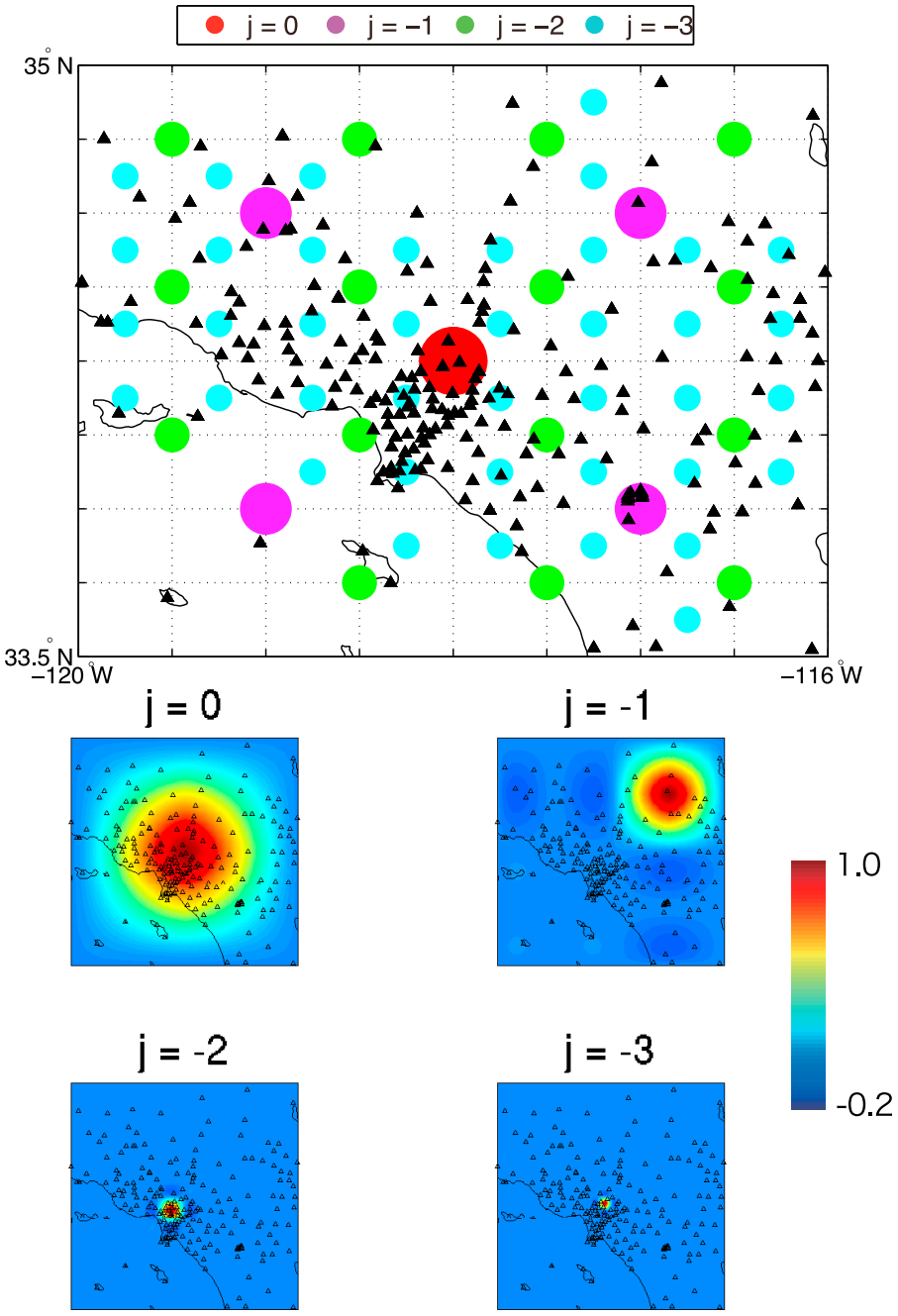

Figure 4. The distribution of wavelet translations used at the different spatial scales in the SCIGN synthetic test. Small panels show examples of the two-dimensional Deslauriers-Dubuc diagonal wavelets for the $j = 0, -1, -2, -3$ scales at a particular translation. (top) The positions of various translations that were selected for the inclusion in the state vector based on the selection criteria for being well observed. The different color circles indicate different scales, j (red, 0; magenta, −1; green, −2; cyan, −3). Black triangles indicate the location of the GPS stations. Note that there are fewer wavelets where the station density is sparse. Each horizontal axis is regularized to a dyadic scale.

values of λ^2 (say 0.001) the filter maps the (large amplitude) secular signal into the transient field (because it has larger a priori uncertainty), which in turn forces α to increase rapidly (Figure 6). In contrast, when λ^2 is larger, α tends to drift toward lower values (consistent with steady deformation) until soon after the onset of the transient (roughly 2002.0). Our synthetic experiments have indicated that choosing a value of λ^2 that is at or slightly larger than the inflection point in the tradeoff curve (Figure 5) leads to a good recovery of the true transient signal. Figure 7 compares the estimated transient displacement field at the final epoch for three values of λ^2 that bracket the inflection point in the tradeoff curve. Below the inflection point ($\lambda^2 = 0.05$) the recovered signal is a combination of the secular and transient fields, while at the

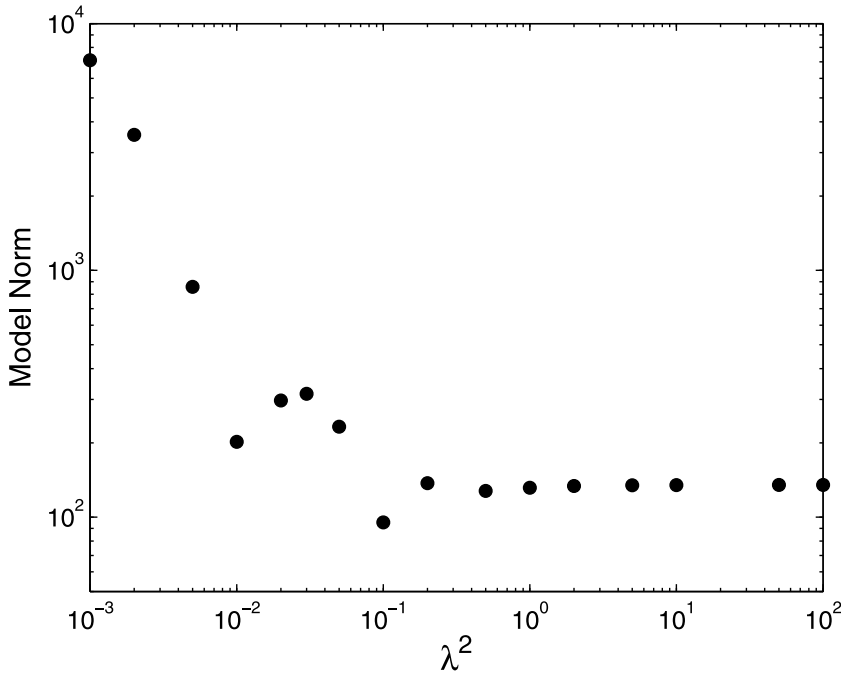

Figure 5. The model norm of the transient strain field at the final epoch for the synthetic data set as estimated by the filter for different values of the spatial smoothing parameter λ^2.

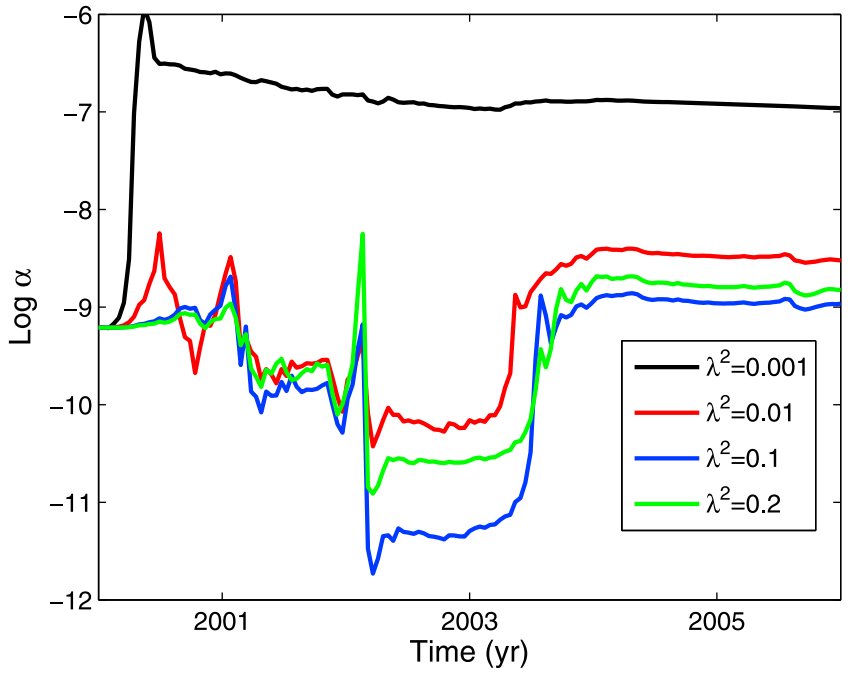

Figure 6. Estimated values of α determined by the forward run of the filter on the synthetic data set as a function of time (epoch) for various values of λ^2. The estimate plotted at a particular time uses all data from previous times. The estimate at the final epoch is applied to all epochs as part of the backsmoothing run of the filter. When the spatial damping is too small (e.g., $\lambda^2 = 0.001$) the filter immediately increases the value of α to allow the secular field to be mapped into the transient term. For more appropriate values of λ^2 the estimate of α decreases (as the filter accumulates evidence of the lack of a transient) until the transient displacement rate reaches its peak (between 2003 and 2004) when the estimate of α is forced to increase abruptly by the data. The variations between about 2000 and 2003 result from the filter converging on a well constrained estimate of α to separate the transient motion under the smoothing constraint and do not reflect an actual transient in the data set. They result from the large amount of a priori uncertainty given to the value of α.

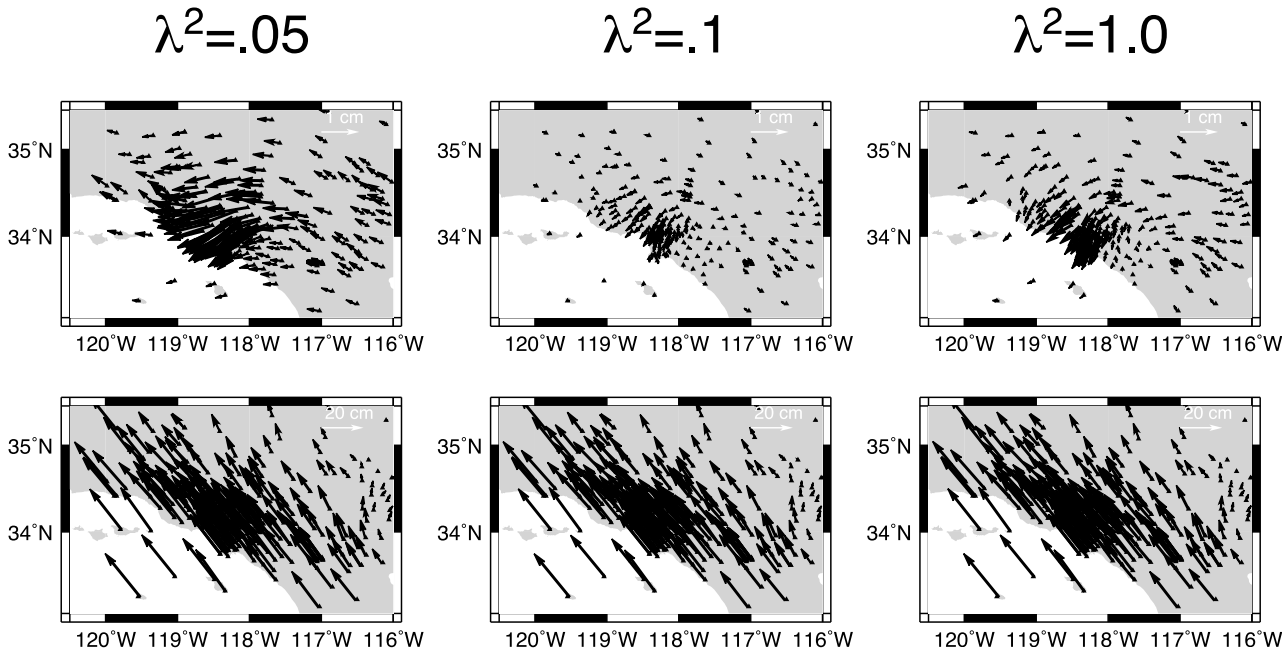

Figure 7. The estimated transient displacement field (top left) for a value of $\lambda^2 = 0.05$ at the final epoch just below the inflection point in Figure 5, (top middle) for a value at the inflection point ($\lambda^2 = 0.1$), and (top right) for a value above the inflection point (λ^2=1.0). (left) The transient signal is highly contaminated by the much larger amplitude secular field, whereas for the appropriate choice of λ^2 the estimated transient agrees well with the input transient (compare to Figure 3). For a larger value ($\lambda^2 = 1$) the transient is oversmoothed in space. (bottom) The estimated secular field for each value of λ^2.

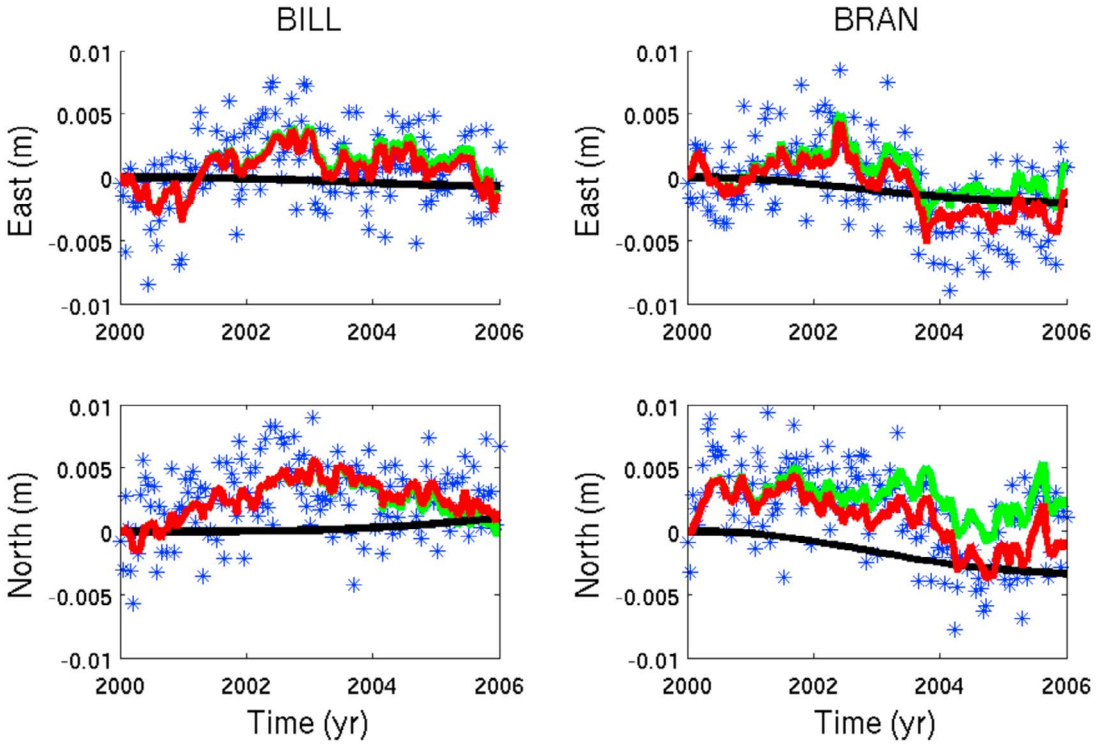

Figure 8. Synthetic GPS time series for the stations BILL and BRAN shown in Figure 3. The filtered estimate of the secular velocity has been subtracted from the synthetic data (blue asterisks). The black curve denotes the backsmoothed estimate of the transient displacement, and the green curve denotes the estimated benchmark term for each component. The red curve is the sum of the black and green curves and shows the overall fit to the data.

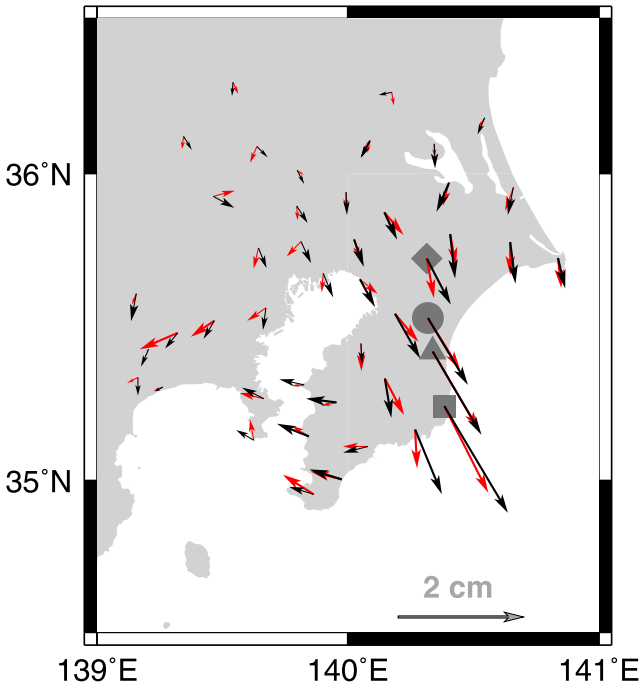

Figure 9. The 1996 Boso Peninsula transient event. Map showing the transient displacement field estimated by differencing the mean station positions from one month of data before and after the event (red arrows) and the transient displacement field estimated by the filter at the final epoch (black arrows). Stations CHIO, CHOE, OOAM, and TOMI are shown as a square, triangle, circle, and diamond.

inflection point ($\lambda^2 = 0.1$) the filter has properly separated the transient field from the secular field (Figure 7).

[36] The filter's success in identifying the transient for $\lambda^2 = 0.1$ results from the spatial coherence of the transient signal. Through the update equations of the Kalman filter, when the transient displacement begins to increase strongly around the middle of the data set (2003.0) the growing residual between the current estimate of the state vector and the data gets mapped into an increase in α, and hence into an increase in the magnitude of the estimated transient signal. This behavior is very similar to that seen in the NIF employing both synthetic and real data sets [*McGuire and Segall*, 2003]. Figure 8 shows examples of the estimated transient (black curves) and benchmark motion terms (green curves) for a station in the middle of the transient region (BRAN, middle white triangle in Figure 3) and a station far removed from the transient (BILL, southeastern white triangle in Figure 3). The simulated data in Figure 8 has had the estimated secular velocity removed from each component so the sum of the transient field and the benchmark term (shown by the red curve) is effectively a measure of the fit to the data. Both stations have drifts of ~5 mm over time periods of a few years due to the benchmark wobble term. For station BILL, the filter properly maps this motion into the benchmark term (green curve) rather than the transient term because this motion is not spatially coherent. For station BRAN, the ~5 mm transient motion to the southwest is properly mapped into the estimated transient field because it is spatially coherent with nearby stations (Figure 3). The success of the filter in this case is encouraging given that the amplitude of the signal (~5 mm) was similar to that of the colored noise at a given station, given the long duration of the simulated transient.

4. Application to the 1996 Boso Slow Earthquake

[37] In May of 1996, anomalous transient displacements were observed in the Japanese continuous GPS array, GEONET, deployed by the Geographical Survey Institute (GSI) of Japan [*Ozawa et al.*, 2003; *Sagiya*, 2004a, 2004b]. Similar slow slip events were also observed in 2002 and 2007 [*Ozawa et al.*, 2007]. The stations exhibiting transient motion cover the whole Boso Peninsula, extending about a 100 km by 100 km area (Figure 9). The time series in and around the Boso Peninsula clearly shows that the GPS stations exhibit gradual movement toward the southeast, with amplitudes of up to ~10 mm and a duration of about 10 days. The amplitude decreases with distance from the station CHIO (the southeast station in Figure 9, shown by a square) suggesting that the source is located offshore of CHIO. Several studies concluded that this transient deformation resulted from aseismic slip on the interface between the subducting Pacific plate and the overlying plate [*Ozawa et al.*, 2003; *Sagiya*, 2004a, 2004b].

[38] We used GPS data around the Boso peninsula recorded by GEONET to test the capability of the NSF for automated detection of this transient. We used 47 GPS stations (Figure 9), with 104 daily position determinations from 1 April to 13 July in 1996, including approximately 40 days before and after the transient event. The daily station coordinates are those obtained through routine analysis of the Geographical Survey Institute of Japan [*Hatanaka et al.*, 2003; *Geographical Survey Institute*, 2004]. Routine GEONET analysis divides the network into regional subnetworks; stations around the Boso peninsula belong to the "south Kanto-Tokai district" that consists of the same antenna-receiver-monument type. This avoids errors due to different antenna phase center variations. Here, we chose stations around the south Kanto district, excluding the more distant stations in the Tokai district.

[39] We applied the NSF to the GEONET data using the same procedure as for the simulation. Because of the relatively small area, we only consider the translational components in the reference frame errors. For this relatively short data set, neither secular displacements nor seasonal variations are significant. The DD wavelet function of the degree 3 is employed as a basis, and only horizontal components of the time series are analyzed.

[40] We determined an appropriate value of the spatial smoothing parameter λ^2 following the same method as in the synthetic test. The tradeoff curve (Figure 10) is similar to the synthetic example (Figure 5) and we choose $\lambda^2 = 2$ as the best estimate. The abrupt nature of this transient results in a very clear increase in the temporal smoothing parameter α at 1996.38 for all values of λ^2 (Figure 11). Owing to the short duration of the data set, we set the prior variance on the secular term to be very small (25 $(\text{mm/yr})^2$) as this would not be well resolved. The estimated secular displacements over the time period are typically about 1mm and their removal leads to the flat baselines seen in Figure 12. The scale factors, σ and τ, were set to 5 and 10 $\text{mm}/\sqrt{year}$, based on inspection of the time series. The minimum scale of -2 was determined

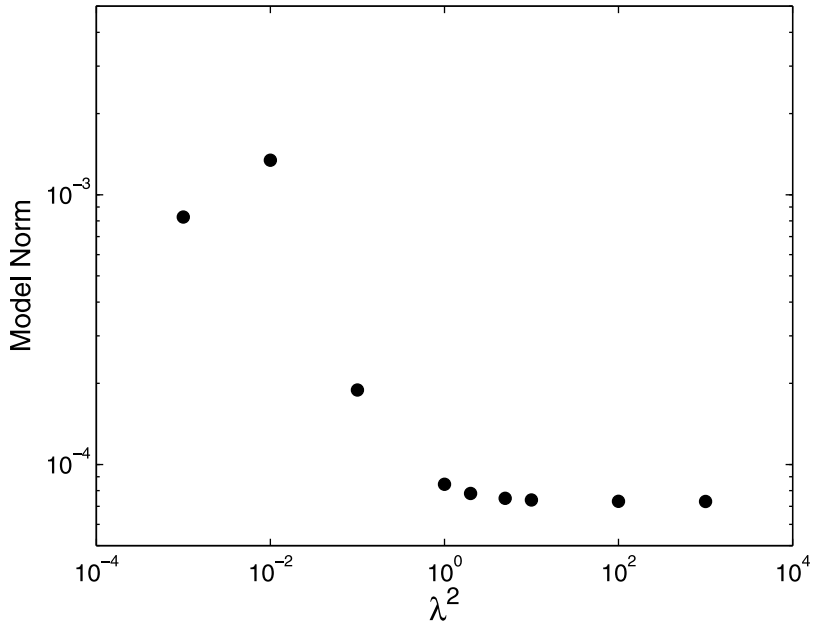

Figure 10. The model norm of the transient strain field at the final epoch for the Boso data set as estimated by the filter for different values of the spatial smoothing parameter λ^2.

to be sufficient to represent the transient field for this relatively small array.

[41] The time history of the estimated transient signal is illustrated in Figure 12 for several stations. The variation in the amplitude of the inferred transient signal from station to station is consistent with the data. However the transient is stretched out over a longer time period from roughly 1996.33 to 1996.40 than the data. The estimated transient field in Figure 12 begins before the actual transient due to the backsmoothing process in the filter algorithm. The signal is oversmoothed in the time domain because one value of α is assumed to apply to the entire data set, which is transient free for the first and last 40 days. Clearly an implementation that allows for a time variable α, such as the particle filter approach used by *Fukuda et al.* [2004], would be necessary to accurately recover the abrupt time history of the transient. However, for the purpose of detecting the transient, the ~1 week bias in oversmoothing is not a significant

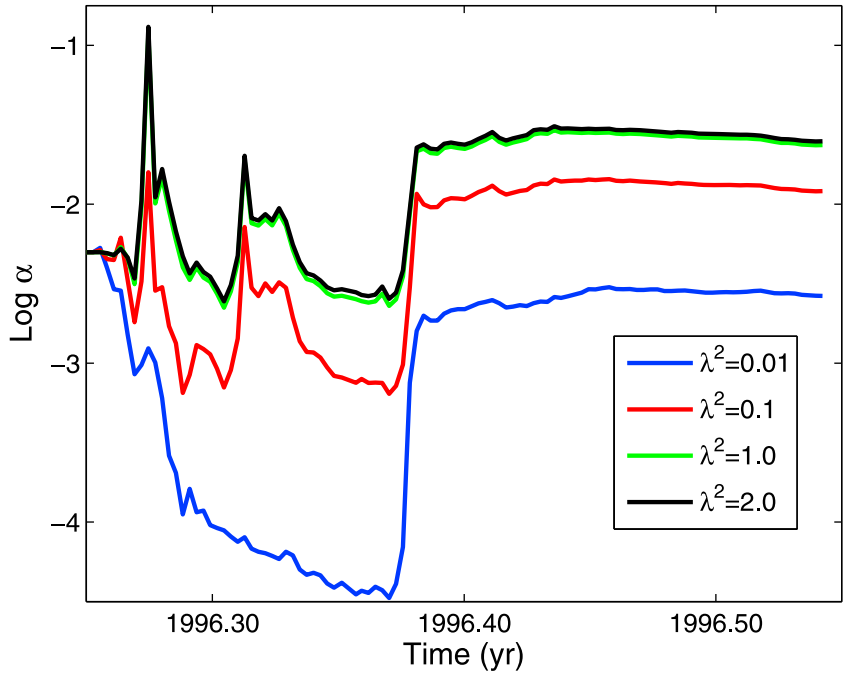

Figure 11. The estimate of α determined by the forward run of the filter, similar to Figure 6, on the Boso data set as a function of time for various values of λ^2.

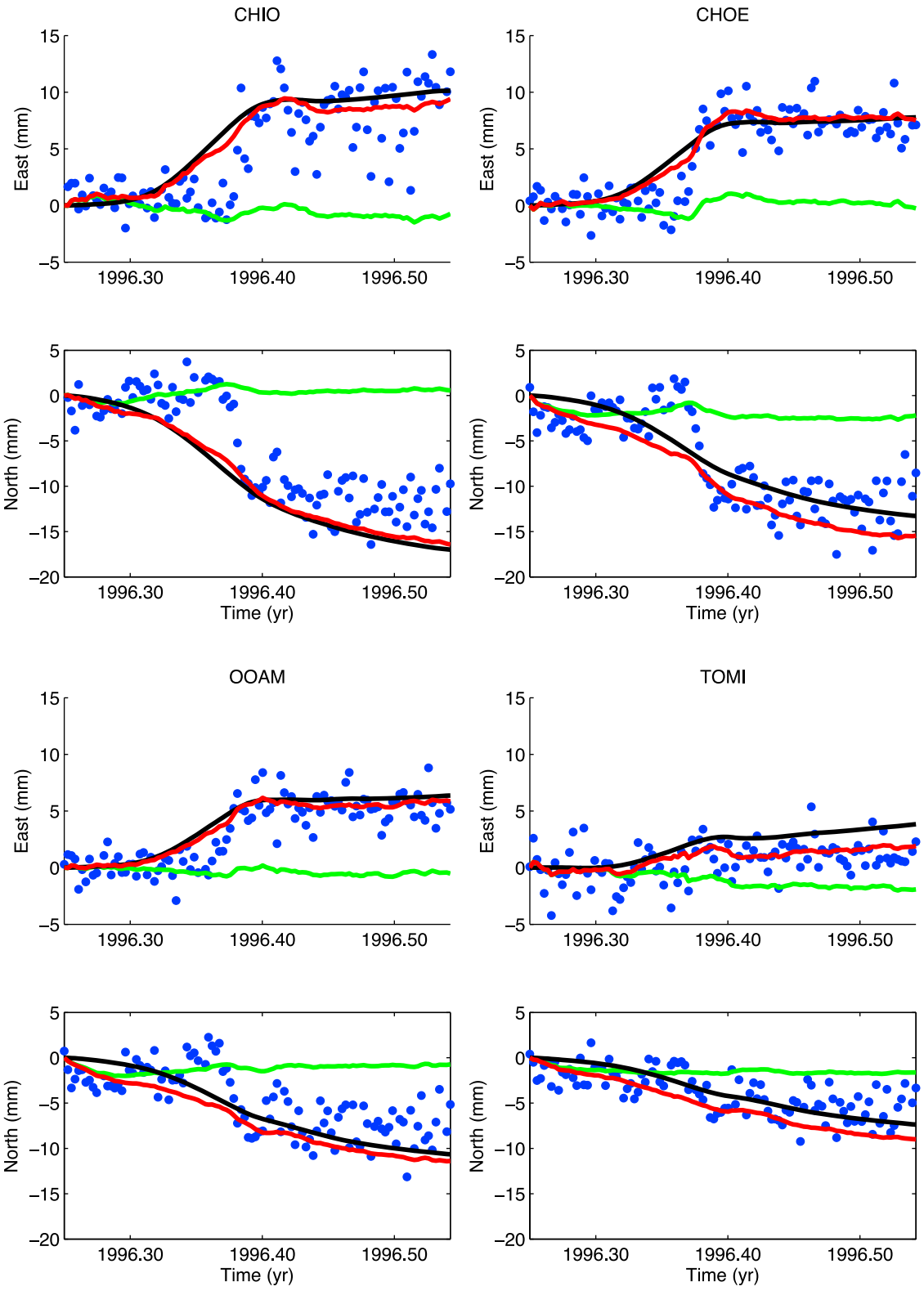

Figure 12. Time series of displacement at four GEONET stations (CHIO, CHOE, OOAM, TOMI) in (top) east and (bottom) north for raw data (blue dots) with the estimated secular trend removed. The estimated transient signal (black line), benchmark motion (green line), are shown as in Figure 8. See Figure 9 for the location of the stations. The red line is the sum of the black and green curves and shows the fit to the data.

drawback. Overall the transient is well localized in both space (Figure 9) and time (Figure 12), demonstrating the ability of the NSF to find such events in real data sets.

5. Discussion

[42] Results presented in the previous sections show that a combination of wavelets with Kalman filtering techniques enables us to separate spatially coherent transient signals from secular motions and localized, colored noise processes, without introducing source-specific models. An important application of the NSF is to search for subtle signals due to smaller slow earthquakes, which would be useful in systematic mapping of slow earthquakes or similar processes in tectonic regions such as Japan, Cascadia, and California. The algorithm is capable of detecting subtle coherent motions that would be good candidates for further analysis. For example, regions the NSF identified as hosting possible transients could be analyzed using the fault-based Network Inversion Filter. Like the NIF, the NSF takes advantage of information from the whole network simultaneously. This should be superior to methods that treat individual time series separately and subsequently search for spatial coherence. Additionally, all of the parameters including secular velocity are estimated simultaneously rather than having to be removed ahead of time which may introduce spurious transients.

[43] As seen in the recovered transient time series, for both the simulations and the Boso Peninsula data, there is a tendency for the filter to produce overly smooth estimates of the transient signal. This is a well-known attribute of the stochastic model, which assumes small departures from steady state, equation (3), with a constant temporal smoothing parameter (see discussion by *Segall and Matthews* [1997]). *Fukuda et al.* [2004; 2008] have introduced a Monte Carlo Mixture filter that propagates a discrete representation of the probability density function of α rather than its mean and covariance. Furthermore, α is allowed to evolve based on variations in the data. Such an approach, coupled to the expansion in equation (5), would allow for improved recovery of the transient displacement field.

Appendix A: Multiresolution Analysis

[44] With a multiresolution analysis (MRA) the space of all square integrable functions in p dimensions, $L^2(\Re^p)$, is subdivided into nested subspaces spanned by a set of scaling functions [see *Mallet*, 1998]. Define the subspace of $L^2(\Re^p)$ spanned by a family of scaling function at a given scale j as

$$V_j = \overline{\underset{\vec{k}}{\mathrm{Span}}\{\phi_{j,\vec{k}}(\vec{x})\}} \quad \vec{k} = \left(k_1, k_2, \cdots k_p\right) \quad k_i \in \boldsymbol{Z}, \tag{A1}$$

where the over bar denotes closure and $\boldsymbol{Z}$ is the set of integers (Figure A1). In short, V_j represents the subspace spanned by all the translations of the scaling function at scale j. MRA requires that the subspaces are nested,

$$V_j \subset V_{j-1} \quad j \in \boldsymbol{Z} \tag{A2}$$

with

$$V_\infty = \{0\}, \quad V_{-\infty} = L^2(\Re^p). \tag{A3}$$

The subspace spanned by analyzing wavelet at scale j, W_j, is such that

$$V_{j-1} = V_j \oplus W_j. \tag{A4}$$

In other words, the space spanned by the scaling function at scale $j-1$, is the sum of the subspace spanned by the scaling function and analyzing wavelet at scale j (Figure A1). This result readily extends to

$$V_{j-2} = V_j \oplus W_j \oplus W_{j-1}. \tag{A5}$$

It is easily seen that by combining equations (A1) to (A4)

$$\begin{aligned} L^2(\Re^p) &= V_j \oplus W_j \oplus W_{j-1} \oplus \cdots \\ &= \cdots \oplus W_{j+2} \oplus W_{j+1} \oplus W_j \oplus W_{j-1} \oplus W_{j-2} \oplus \cdots. \end{aligned} \tag{A6}$$

Any square integrable function can be represented by a linear combination of scaling functions at the largest scale, and a linear combination of analyzing wavelets at all smaller scales. Note that the subspace spanned by the scaling functions at scale j contains all subspaces spanned by analyzing wavelets at larger scales. This is reflected for the one-dimensional case in equation (8) and is illustrated for a one-dimensional series in Figure A2.

Appendix B: Wavelets in Two Dimensions

[45] Following the convention of *Mallet* [1998], define scaling functions and analyzing wavelets $\Psi^i(x_1,x_2)$ in two dimensions as

$$\begin{aligned} &\Psi_{j,k_1,k_2}(x_1,x_2) = 2^{-j}\Psi^i\left(2^{-j}x_1 - k_1,\ 2^{-j}x_2 - k_2\right), \\ &\quad j,k_1,k_2 \in \boldsymbol{Z}, \quad i = 1,2,3, \end{aligned} \tag{B1}$$

$$\Phi_{j,k_1,k_2}(x_1,x_2) = 2^{-j}\Phi^0\left(2^{-j}x_1 - k_1,\ 2^{-j}x_2 - k_2\right), \quad j,k_1,k_2 \in \boldsymbol{Z}. \tag{B2}$$

The two-dimensional wavelets can be constructed as the tensor product of one-dimensional wavelets and scaling functions at the same scale.

$$\Psi^1 = \phi(x_1) \cdot \psi(x_2) \equiv \Psi^e(x_1,\ x_2), \tag{B3}$$

$$\Psi^2 = \psi(x_1) \cdot \phi(x_2) \equiv \Psi^n(x_1,\ x_2), \tag{B4}$$

$$\Psi^3 = \psi(x_1) \cdot \psi(x_2) \equiv \Psi^d(x_1,\ x_2), \tag{B5}$$

and

$$\Phi^0 = \phi(x_1) \cdot \phi(x_2) \equiv \Phi^s(x_1,x_2). \tag{B6}$$

Here $\phi(x_1)$ and $\phi(x_2)$ are the one-dimensional scaling functions in the x_1 and x_2 directions, and $\psi(x_1)$ and $\psi(x_2)$ are the one-dimensional analyzing wavelets in x_1 and x_2 directions. We refer to the functions Ψ^e, Ψ^n, and Ψ^d as the east-west,

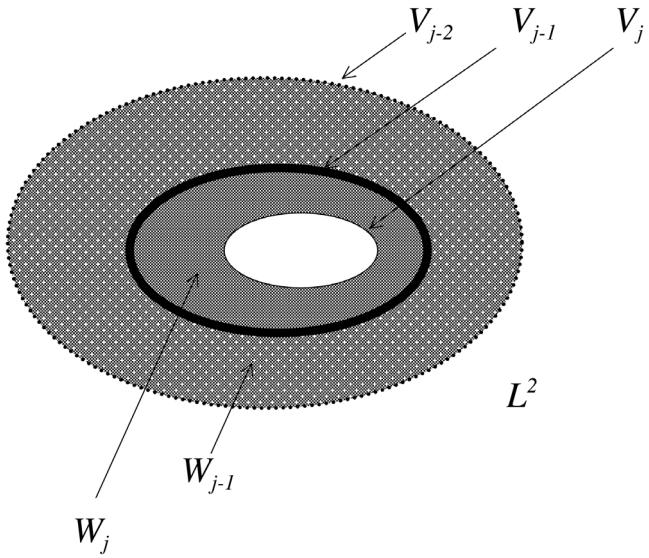

Figure A1. Schematic relation of subspaces between scaling functions and analyzing wavelets. Note that the subspace spanned by the scaling functions at scale $j-1$, V_{j-1} is equivalent to that spanned by the scaling functions V_j and analyzing wavelets W_j at scale j.

north-south, and diagonal wavelets. The scaling function in two dimensions is the tensor product of the two one-dimensional scaling functions.

[46] According to *Mallet* [1998], any square integrable two-dimensional function $g(x_1,x_2)$ can be represented as

$$g(x_1,x_2) = \sum_{k_1=-\infty}^{\infty}\sum_{k_2=-\infty}^{\infty} \Phi^s_{j_0,k_1,k_2}(x_1,x_2)\, c^s_{j_0,k_1,k_2} + \sum_{j=-\infty}^{j_0}\sum_{k_1=-\infty}^{\infty}\sum_{k_2=-\infty}^{\infty}\Big[\Psi^e_{j,k_1,k_2}(x_1,x_2)\, c^e_{j,k_1,k_2} + \Psi^n_{j,k_1,k_2}(x_1,x_2)\, c^n_{j,k_1,k_2} + \Psi^d_{j,k_1,k_2}(x_1,x_2)\, c^d_{j,k_1,k_2}\Big] \quad \text{(B7)}$$

where j_0 is an arbitrarily scale and $c^s_{j_0,k_1,k_2}$, c^e_{j,k_1,k_2}, c^n_{j,k_1,k_2}, c^d_{j,k_1,k_2} are coefficients.

Appendix C: A State Space Modeling

[47] The data at epoch k, $\underline{d}_k$, are related to the state vector $\underline{X}_k$ through the observation equation, which is nonlinear because α is included in the state vector,

$$\underline{d}_k = \underline{h}_k(\underline{X}_k) + \underline{\varepsilon}_k \qquad \underline{\varepsilon}_k \sim N\left(0,\ \underline{\underline{R}}_k\right). \quad \text{(C1)}$$

$\underline{\varepsilon}_k$ is the measurement errors where $\underline{\underline{R}}_k = \sigma^2\underline{\underline{\Sigma}}_{\mathbf{x}}$. In this work, only horizontal displacements are analyzed. The state vector $\underline{X}_k$ consists of quantities that describe the underlying processes of the system as follows:

$$\underline{X}_k = \Big[c_1^{(e)}, \dot{c}_1^{(e)}, \cdots, c_M^{(e)}, \dot{c}_M^{(e)}, c_1^{(n)}, \dot{c}_1^{(n)}, \cdots, c_M^{(n)}, \dot{c}_M^{(n)}, v_1^{(e)}, \cdots, v_N^{(e)}, v_1^{(n)}, \cdots, v_N^{(n)}, L_1^{(e)}, \cdots, L_N^{(e)}, L_1^{(n)}, \cdots, L_N^{(n)}, F_1^{(e)}, F_1^{(n)}, \alpha\Big]^T, \quad \text{(C2)}$$

where M is the number of basis functions and N is the number of stations. (e) and (n) denote east and north components, respectively. Here only translation component is considered for the reference frame errors. The total number of state vector elements is 2*2*M+2*N+2*N+2*1+1. The observation equation includes our model for the GPS time series (equation (1)). In the NIF, it has sometimes been augmented with additional "pseudodata" for enforcing positivity or smoothing constraints [*McGuire and Segall*, 2003]. However, there are no nonlinear constraints that need to be enforced in this manner in our current implementation of the NSF.

[48] The state transition equation propagates the state vector and its covariance matrix forward in time and is a simple linear equation for our chosen stochastic models for L and c.

$$\underline{X}_{k+1|k} = \underline{\underline{T}}_k \cdot \underline{X}_k + \underline{\delta}_k \qquad \underline{\delta}_k \sim N\left(0,\ \underline{\underline{Q}}_k\right)$$
$$\Sigma_{k+t|k} = \underline{\underline{T}}_k \cdot \underline{X}_k \cdot \underline{\underline{T}}_k^{\mathrm{T}} \quad \text{(C3)}.$$

Here the matrix $\underline{\underline{T}}_k$ is the state transition matrix that predicts the state of system at epoch $k+1$ from the previous epoch k, and $\underline{\underline{Q}}_k$ is the covariance matrix of the process noise accounting for statistical variability in the system. These matrices are specified by stochastic process assigned for the various elements of the state vector.

[49] Given the observation equation (C1) and the predicted values of the state vector and its covariance from equation (C3), the extended Kalman filter update equations can be used to incorporate the current data into the estimate of the state vector,

$$\underline{X}_{k+1|k+1} = \underline{X}_{k+1|k} + \underline{\underline{K}}_{k+1} \cdot \underline{\nu}_{k+1}, \quad \text{(C4)}$$

$$\underline{\underline{K}}_{k+1} = \underline{\underline{\Sigma}}_{k+1|k} \cdot \underline{\underline{H}}_{k+1}^T \cdot \left(\underline{\underline{R}}_{k+1} + \underline{\underline{H}}_{k+1} \cdot \underline{\underline{\Sigma}}_{k+1|k} \cdot \underline{\underline{H}}_{k+1}^T\right)^{-1}, \quad \text{(C5)}$$

$$\underline{\nu}_{k+1} = \underline{d}_k - \underline{h}_{k+1}\left(\underline{X}_{k+1|k}\right). \quad \text{(C6)}$$

By iterating the prediction and update steps, one can proceed through the data set to determine the best estimate of the state vector at each epoch given all of the data up to that point. It is often desirable to determine the best estimate of the state vector at a given epoch given all of the data (from both before and after that epoch). This estimate is determined by effectively running the filter backward in time using an efficient algorithm known as the Kalman smoother [see *Rauch et al.*, 1965; *Segall and Matthews*, 1997]. The time series of the transient component deformation shown in Figures 8 and 12 are these backsmoothed estimates.

[50] **Acknowledgments.** We thank L. Zhen for producing the synthetic GPS data used in simulations, the Geographical Survey Institute of Japan for the GPS data access, and A. Morimoto for useful information about wavelets. We thank the Grant-in-Aid for Young Scientists [KAKENHI(18740283)] of the Ministry of Education, Culture, Sports, Science and Technology of Japan and the postdoctoral fellowships for research abroad of the Japan Society for the Promotion of Science. We also acknowledge support from NASA grant NNG04GC93G. This research was supported by the Southern California Earthquake Center. SCEC is funded by NSF Cooperative Agreement EAR-0529922 and USGS Cooperative

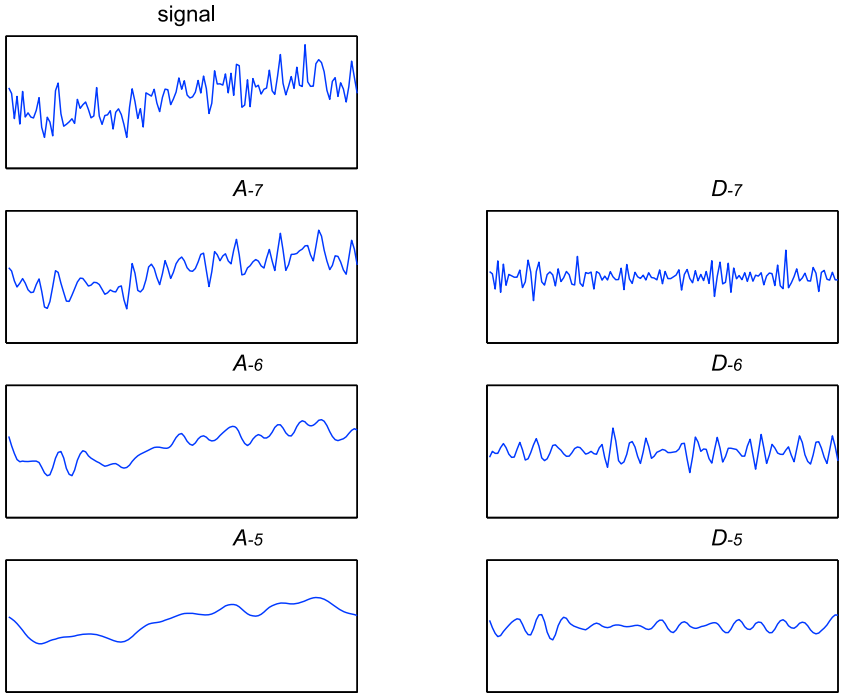

Figure A2. An example of the relationship between scaling functions and analyzing wavelets for multiresolution analysis of a signal. The original signal consisting of 2^8 data points is decomposed into a component (A_{-7}) represented by a linear combination of scaling functions V_{-7}, and a component (D_{-7}) represented by a linear combination of analyzing wavelets W_{-7}, at scale $j = -7$. Note that the independent variable for all of our wavelets is in space, and no wavelets are used in the time domain in this paper. The component A_{-7} can be further expressed with larger spatial scale components of scaling functions and analyzing wavelets. For example, the component A_{-7} can be further decomposed into A_{-6} and D_{-6}. Thus, the original signal can be represented by the sum of A_{-6}, D_{-6}, and D_{-7}.

Agreement 07HQAG0008. The SCEC contribution number for this paper is 1332. We used the Wavelab package to calculate wavelets. R.O. is grateful for continuous support from the members of the tectono-hydrology research team of the Geological Survey of Japan.

References

Addison, P. (2002), *The Illustrated Wavelet Transform Handbook: Introductory Theory and Applications in Science, Engineering, Medicine and Finance*, 353 pp, Inst. of Physics, London.

Aoki, Y., P. Segall, T. Kato, P. Cervelli, and S. Shimada (1999), Upward dike migration during the 1997 seismic swarm off the Izu Peninsula, Japan, from inversion of deformation data, *Science*, *286*, 927–930.

Brooks, B. A., J. H. Foster, M. Bevis, L. N. Frazer, C. J. Wolfe, and M. Behn (2006), Periodic slow earthquakes on the flank of Kilauea volcano, Hawaii, *Earth Planet. Sci. Lett.*, *246*(3–4), 207–216.

Brown, R. G., and P. Hwang (1997), *Introduction to Random Signals and Applied Kalman Filtering*, 496 pp., John Wiley, New York.

Brudzinski, M. R., and R. M. Allen (2007), Segmentation in episodic tremor and slip all along Cascadia, *Geology*, *35*, 907–910.

Bürgmann, R., S. Ergintav, P. Segall, E. Hearn, S. McClusky, R. E. Reilinger, H. Woith, and J. Zschau (2002), Time-dependent distributed afterslip on and deep below the Izmit earthquake rupture, *Bull. Seismol. Soc. Am.*, *92*, 126–137.

Cervelli, P., P. Segall, K. Johnson, M. Lisowski, and A. Miklius (2002), Sudden aseismic fault slip on the south flank of Kilauea volcano, *Nature*, *415*, 1014–1018.

Daubechies, I. (1992), *Ten Lectures on Wavelets*, CBMS-NSF Regional Conference Series, *Appl. Math.*, 377 pp., Soc. for Ind. and Appl. Math., Philadelphia, Pa.

Delahaye, E. J., J. Townend, M. E. Reyners, and G. Rogers (2009), Microseismicity but no tremor accompanying slow slip in the Hikurangi subduction zone, New Zealand, *Earth Planet. Sci. Lett.*, *277*(1/2), 21–28.

Douglas, A., J. Beavan, L. Wallace, and J. Townend (2005), Slow slip on the northern Hikurangi subduction interface, New Zealand, *Geophys. Res. Lett.*, *32*, L16305, doi:10.1029/2005GL023607.

Dragert, H., K. Wang, and T. S. James (2001), A silent slip event on the deeper Cascadia subduction interface, *Science*, *292*, 1525–1528.

Fukuda, J., T. Higuchi, S. Miyazaki, and T. Kato (2004), A new approach to time-dependent inversion of geodetic data using a Monte Carlo mixture Kalman filter, *Geophys. J. Int.*, *159*, 17–39.

Fukuda, J., S. Miyazaki, T. Higuchi, and T. Kato (2008), Geodetic inversion for space-time distribution of fault slip with time-varying smoothing regularization, *Geophys. J. Int.*, *173*, 25–48.

Geographical Survey Institute (2004), Establishment of the nationwide observation system of 1,200 GPS-based control stations, *J. Geogr. Surv. Inst.*, *103*, 3–51, (in Japanese).

Hatanaka, Y., T. Iizuka, M. Sawada, A. Yamagiwa, Y. Kikuta, J. M. Johnson, and C. Rocken (2003), Improvement of the analysis strategy of GEONET, *J. Geogr. Surv. Inst.*, *49*, 11–37.

Heki, K., S. Miyazaki, and H. Tsuji (1997), Silent fault slip following an interplate thrust earthquake at the Japan Trench, *Nature*, *386*, 595–598.

Hirose, H., and K. Obara (2005), Repeating short- and long-term slow slip events with deep tremor activity around the Bungo Channel region, southwest Japan, *Earth Planets Space*, *57*, 961–972.

Hirose, H., and K. Obara (2006), Short-term slow slip and correlated tremor episodes in the Tokai region, central Japan, *Geophys. Res. Lett.*, *33*, L17311, doi:10.1029/2006GL026579.

Hirose, H., K. Hirahara, F. Kimata, N. Fujii, and S. Miyazaki (1999), A slow thrust slip event following the two 1996 Hyuganada earthquakes beneath the Bungo Channel, southwest Japan, *Geophys. Res. Lett.*, *26*(21), 3237–3240, doi:10.1029/1999GL010999.

Hsu, Y. J., et al. (2006), Frictional afterslip following the 2005 Nias-Simeulue earthquake, Sumatra, *Science*, *312*(5782), 1921–1926.

Hsu, Y.-J., P. Segall, S.-B. Yu, L.-C. Kuo, and C. A. Williams (2007), Temporal and spatial variations of post-seismic deformation following the 1999 Chi-Chi, Taiwan earthquake, *Geophys. J. Int.*, 169, doi:10.1111/j.1365-246X.2006.03310.x.

Hudnut, K. W., Y. Bock, J. E. Galetzka, F. H. Webb, and W. H. Young (2002), The Southern California Integrated GPS Network (SCIGN), in *Seismotectonics in Convergent Plate Boundary*, edited by Y. Fujinawa, and A. Yoshida, 167–189, Terrapub, Tokyo, Japan.

Kostoglodov, V., S. K. Singh, J. A. Santiago, K. M. Larson, A. R. Lowry, and R. Bilham (2003), A large silent earthquake in the Guerrero seismic gap, Mexico, *Geophys. Res. Lett.*, *30*(15), 1807, doi:10.1029/2003GL017219.

Kumar, P., and E. Foufoula-Georgiou (1994), Wavelet analysis in geophysics: An introduction, in *Wavelets in Geophysics*, edited by E. Foufoula-Georgiou, and P. Kumar, pp. 1–43, Academic, San Diego, Calif.

Kumar, P., and E. Foufoula-Georgiou (1997), Wavelet analysis for geophysical applications, *Rev. Geophys.*, *35*(4), 385–412, doi:10.1029/97RG00427.

Larson, K. M., V. Kostoglodov, S. Miyazaki, and J. A. Santiago (2007), The 2006 aseismic slow slip event in Guerrero, Mexico: New results from GPS, *Geophys. Res. Lett.*, *34*, L13309, doi:10.1029/2007GL029912.

Linde, A. T., K. Ágústsson, I. S. Sacks, and R. Stefánsson (1993), Mechanism of the 1991 eruption of Hekla from continuous borehole strain monitoring, *Nature*, *365*, 737–740.

Linde, A. T., M. Gladwin, M. Johnston, R. Gwyther, and R. Bilham (1996), A slow earthquake sequence on the San Andreas Fault, *Nature*, *383*, 65–68.

Lowry, A. R., K. M. Larson, V. Kostoglodov, and R. Bilham (2001), Transient fault slip in Guerrero, southern Mexico, *Geophys. Res. Lett.*, *28*(19), 3753–3756, doi:10.1029/2001GL013238.

Mallet, S. (1998), *A Wavelet Tour of Signal Processing*, 2nd ed., pp. 637, Academic, New York.

McCaffrey, R., L. M. Wallace, and J. Beavan (2008), Slow slip and frictional transition at low temperature at the Hikurangi subduction zone, *Nat. Geosci.*, *1*, 316–320.

McGuire, J. J., and P. Segall (2003), Imaging of aseismic fault slip transients recorded by dense geodetic networks, *Geophys. J. Int.*, *155*, 778–788.

Miller, M. M., T. Melbourne, D. J. Johnson, and W. Q. Sumner (2002), Periodic slow earthquakes from the Cascadia subduction zone, *Science*, *295*, 2423, doi:10.1126/science.1071193.

Miyazaki, S., J. J. McGuire, and P. Segall (2003), A transient subduction zone slip episode in southwest Japan observed by the nationwide GPS array, *J. Geophys. Res.*, *108*(B2), 2087, doi:10.1029/2001JB000456.

Miyazaki, S., P. Segall, J. J. McGuire, T. Kato, and Y. Hatanaka (2006), Spatial and temporal evolution of stress and slip rate during the 2000 Tokai slow earthquake, *J. Geophys. Res.*, *111*, B03409, doi:10.1029/2004JB003426.

Miyazaki, S., and K. Larson (2008), Coseismic and early postseismic slip for the 2003 Tokachi-oki earthquake sequence inferred from GPS data, *Geophys. Res. Lett.*, *35*, L04302, doi:10.1029/2007GL032309.

Murray, J. R., and P. Segall (2005), Spatiotemporal evolution of a transient slip event on the San Andreas Fault near Parkfield, California, *J. Geophys. Res.*, *110*, B09407, doi:10.1029/2005JB003651.

Niemi, N., B. Wernicke, A. Friedrich, M. Simons, R. Bennett, and J. Davis (2004), BARGEN continuous GPS data across the eastern Basin and Range province, and implications for fault system dynamics, *Geophys. J. Int.*, *159*, 842–862.

Norabuena, E., et al. (2004), Geodetic and seismic constraints on some seismogenic zone processes in Costa Rica, *J. Geophys. Res.*, *109*, B11403, doi:10.1029/2003JB002931.

Obara, K. (2002), Nonvolcanic deep tremor associated with subduction in southwest Japan, *Science*, *296*, 1679–1681.

Owen, S., P. Segall, M. Lisowski, A. Miklius, R. Denlinger, and M. Sako (2000), Rapid deformation of Kilauea volcano: GPS measurements between 1990 and 1996, *J. Geophys. Res.*, *105*(B8), 18,983–18,998, doi:10.1029/2000JB900109.

Ozawa, S., M. Murakami, and T. Tada (2001), Time-dependent inversion study of the slow thrust event in the Nankai Trough subduction zone, southwestern Japan, *J. Geophys. Res.*, *106*(B1), 787–802, doi:10.1029/2000JB900317.

Ozawa, S., M. Murakami, M. Kaidzu, T. Tada, Y. Hatanaka, H. Yarai, and T. Nishimura (2002), Detection and monitoring of ongoing aseismic slip in the Tokai region, central Japan, *Science*, *298*, 1009–1012.

Ozawa, S., S. Miyazaki, Y. Hatanaka, T. Imakiire, M. Kaidzu, and M. Murakami (2003), Characteristic silent earthquakes in the eastern part of the Boso peninsula, Central Japan, *Geophys. Res. Lett.*, *30*(6), 1283, doi:10.1029/2002GL016665.

Ozawa, S., et al. (2005), Transient crustal deformation in Tokai region, central Japan, until May 2004, *Earth Planets Space*, *57*, 909–915.

Ozawa, S., H. Suito, and M. Tobita (2007), Occurrence of quasi-periodic slow-slip off the east coast of the Boso peninsula, Central Japan, *Earth Planets Space*, *59*, 1241–1245.

Pritchard, M. E., and M. Simons (2006), An aseismic slip pulse in northern Chile and along-strike variations in seismogenic behavior, *J. Geophys. Res.*, *111*, B08405, doi:10.1029/2006JB004258.

Rauch, H. E., F. Tung, and C. T. Striebel (1965), Maximum likelihood estimates of linear dynamic systems, *AIAA J.*, *3*, 1445–1450.

Rogers, G., and H. Dragert (2003), Episodic tremor and slip on the Cascadia subduction zone: The chatter of silent slip, *Science*, *300*, 1942–1943.

Sagiya, T. (2004a), Interplate coupling in the Kanto District, central Japan, and the Boso Silent earthquake in May 1996, *Pure Appl. Geophys.*, *161*, 2327–2342.

Sagiya, T. (2004b), A decade of GEONET: 1994–2003—The continuous GPS observation in Japan and its impact on earthquake studies, *Earth Planets Space*, *56*, 29–41.

Schwartz, S., and J. Rokosky (2007), Slow slip events and seismic tremor at circum-Pacific subduction zones, *Rev. Geophys.*, *45*, RG3004, doi:10.1029/2006RG000208.

Segall, P., and M. Matthews (1997), Time-dependent inversion of geodetic data, *J. Geophys. Res.*, *102*(B10), 22,391–22,409, doi:10.1029/97JB01795.

Segall, P., R. Bürgmann, and M. Matthews (2000), Time-dependent triggered afterslip following the 1989 Loma-Prieta earthquake, *J. Geophys. Res.*, *105*(B3), 5615–5634, doi:10.1029/1999JB900352.

Segall, P., and J. L. Davis (1997), GPS applications for geodynamics and earthquake studies, *Annu. Rev. Earth Planet. Sci.*, *25*, 301–336.

Segall, P., E. K. Desmarais, D. Shelly, A. Miklius, and P. Cervelli (2006), Earthquakes triggered by silent slip events on Kilauea Volcano, Hawaii, *Nature*, *442*, 71–74, doi:10.1038/nature04938.

Shelly, D. R., G. C. Beroza, and S. Ide (2007), Nonvolcanic tremor and low-frequency earthquake swarms, *Nature*, *446*, 305–307.

Sweldens, S., and P. Schröder (1996), Building your own wavelets at home, in *Wavelets: Computer Graphics*, pp. 15–87. (Available at http://www.multires.caltech.edu/teaching/courses/waveletcourse/)

Szeliga, W., T. Melbourne, M. Santillan, and M. Miller (2008), GPS constraints on 34 slow slip events within the Cascadia subduction zone, 1997–2005, *J. Geophys. Res.*, *113*, B04404, doi:10.1029/2007JB004948.

Tape, C., P. Muse, M. Simons, D. Dong, and F. Webb (2009), Multiscale estimation of GPS velocity fields, *Geophys. J. Int.*, *179*, 945–971.

Wang, K., H. Dragert, H. Kao, and E. Roeloffs (2008), Characterizing an "uncharacteristic" ETS event in northern Cascadia, *Geophys. Res. Lett.*, *35*, L15303, doi:10.1029/2008GL034415.

Wyatt, F. K. (1989), Displacement of surface monuments; vertical motion, *J. Geophys. Res.*, *94*(B2), 1655–1664, doi:10.1029/JB094iB02p01655.

Zhang, J., Y. Bock, H. Johnson, P. Fang, S. Williams, J. Genrich, S. Wdowinski, and J. Behr (1997), Southern California Permanent GPS Geodetic Array: Error analysis of daily position estimates and site velocities, *J. Geophys. Res.*, *102*(B8), 18,035–18,055, doi:10.1029/97JB01380.

J. J. McGuire, Woods Hole Oceanographic Institution, Woods Hole, MA 02543, USA.

R. Ohtani, Geological Survey of Japan, National Institute of Advanced Industrial Science and Technology, Tsukuba, Japan.

P. Segall, Department of Geophysics, Stanford University, CA 94305-2215, USA.